

# Measurement of Neutrino-Induced Neutral-Current Coherent $\pi^0$ Production in the NOvA Near Detector

M. A. Acero,<sup>2</sup> P. Adamson,<sup>12</sup> L. Aliaga,<sup>12</sup> T. Alion,<sup>39</sup> V. Allakhverdian,<sup>27</sup> N. Anfimov,<sup>27</sup> A. Antoshkin,<sup>27,31</sup> E. Arrieta-Diaz,<sup>37</sup> A. Aurisano,<sup>6</sup> A. Back,<sup>24</sup> C. Backhouse,<sup>44</sup> M. Baird,<sup>19,39,45</sup> N. Balashov,<sup>27</sup> P. Baldi,<sup>25</sup> B. A. Bambah,<sup>17</sup> S. Basher,<sup>43</sup> K. Bays,<sup>4,21</sup> B. Behera,<sup>18</sup> S. Bending,<sup>44</sup> R. Bernstein,<sup>12</sup> V. Bhatnagar,<sup>32</sup> B. Bhuyan,<sup>14</sup> J. Bian,<sup>25,31</sup> J. Blair,<sup>16</sup> A.C. Booth,<sup>39</sup> A. Bolshakova,<sup>27</sup> P. Bour,<sup>9</sup> C. Bromberg,<sup>29</sup> N. Buchanan,<sup>8</sup> A. Butkevich,<sup>22</sup> M. Campbell,<sup>44</sup> T. J. Carroll,<sup>42</sup> E. Catano-Mur,<sup>24</sup> S. Childress,<sup>12</sup> B. C. Choudhary,<sup>11</sup> B. Chowdhury,<sup>35</sup> T. E. Coan,<sup>37</sup> M. Colo,<sup>47</sup> L. Corwin,<sup>36</sup> L. Cremonesi,<sup>44</sup> D. Cronin-Hennessy,<sup>31</sup> G. S. Davies,<sup>19</sup> P. F. Derwent,<sup>12</sup> P. Ding,<sup>12</sup> Z. Djurcic,<sup>1</sup> D. Doyle,<sup>8</sup> E. C. Dukes,<sup>45</sup> P. Dung,<sup>42</sup> H. Duyang,<sup>35</sup> S. Edayath,<sup>7</sup> R. Ehrlich,<sup>45</sup> G. J. Feldman,<sup>15</sup> W. Flanagan,<sup>10</sup> M. J. Frank,<sup>34,45</sup> H. R. Gallagher,<sup>43</sup> R. Gandrajula,<sup>29</sup> F. Gao,<sup>33</sup> S. Germani,<sup>44</sup> A. Giri,<sup>18</sup> R. A. Gomes,<sup>13</sup> M. C. Goodman,<sup>1</sup> V. Grichine,<sup>28</sup> M. Groh,<sup>19</sup> R. Group,<sup>45</sup> B. Guo,<sup>35</sup> A. Habig,<sup>30</sup> F. Haki,<sup>20</sup> J. Hartnell,<sup>39</sup> R. Hatcher,<sup>12</sup> A. Hatzikoutelis,<sup>41</sup> K. Heller,<sup>31</sup> A. Himmel,<sup>12</sup> A. Holin,<sup>44</sup> B. Howard,<sup>19</sup> J. Huang,<sup>42</sup> J. Huyen,<sup>12</sup> F. Jediny,<sup>9</sup> C. Johnson,<sup>8</sup> M. Judah,<sup>8</sup> I. Kakorin,<sup>27</sup> D. Kalra,<sup>32</sup> D.M. Kaplan,<sup>21</sup> R. Keloth,<sup>7</sup> O. Klimov,<sup>27</sup> L.W. Koerner,<sup>16</sup> L. Kolupaeva,<sup>27</sup> S. Kotelnikov,<sup>28</sup> A. Kreymer,<sup>12</sup> Ch. Kulenberg,<sup>27</sup> A. Kumar,<sup>32</sup> C. D. Kuruppu,<sup>35</sup> V. Kus,<sup>9</sup> T. Lackey,<sup>19</sup> K. Lang,<sup>42</sup> S. Lin,<sup>8</sup> M. Lokajicek,<sup>23</sup> J. Lozier,<sup>4</sup> S. Luchuk,<sup>22</sup> K. Maan,<sup>32</sup> S. Magill,<sup>1</sup> W. A. Mann,<sup>43</sup> M. L. Marshak,<sup>31</sup> V. Matveev,<sup>22</sup> D. P. Méndez,<sup>39</sup> M. D. Messier,<sup>19</sup> H. Meyer,<sup>46</sup> T. Miao,<sup>12</sup> W. H. Miller,<sup>31</sup> S. R. Mishra,<sup>35</sup> A. Mislivec,<sup>31</sup> R. Mohanta,<sup>17</sup> A. Moren,<sup>30</sup> L. Mualem,<sup>4</sup> M. Muether,<sup>46</sup> K. Mulder,<sup>44</sup> S. Mufson,<sup>19</sup> R. Murphy,<sup>19</sup> J. Musser,<sup>19</sup> D. Naples,<sup>33</sup> N. Nayak,<sup>25</sup> J. K. Nelson,<sup>47</sup> R. Nichol,<sup>44</sup> E. Niner,<sup>12</sup> A. Norman,<sup>12</sup> T. Nosek,<sup>5</sup> Y. Oksuzian,<sup>45</sup> A. Olshevskiy,<sup>27</sup> T. Olson,<sup>43</sup> J. Paley,<sup>12</sup> R. B. Patterson,<sup>4</sup> G. Pawloski,<sup>31</sup> D. Pershey,<sup>4</sup> O. Petrova,<sup>27</sup> R. Petti,<sup>35</sup> R. K. Plunkett,<sup>12</sup> B. Potukuchi,<sup>26</sup> C. Principato,<sup>45</sup> F. Psihas,<sup>19</sup> V. Raj,<sup>4</sup> A. Radovic,<sup>47</sup> R. A. Rameika,<sup>12</sup> B. Rebel,<sup>12,48</sup> P. Rojas,<sup>8</sup> V. Ryabov,<sup>28</sup> K. Sachdev,<sup>12</sup> O. Samoylov,<sup>27</sup> M. C. Sanchez,<sup>24</sup> I. S. Seong,<sup>25</sup> P. Shanahan,<sup>12</sup> A. Sheshukov,<sup>27</sup> P. Singh,<sup>11</sup> V. Singh,<sup>3</sup> E. Smith,<sup>19</sup> J. Smolik,<sup>9</sup> P. Snopok,<sup>21</sup> N. Solomey,<sup>46</sup> E. Song,<sup>45</sup> A. Sousa,<sup>6</sup> K. Soustruznik,<sup>5</sup> M. Strait,<sup>31</sup> L. Suter,<sup>12</sup> R. L. Talaga,<sup>1</sup> P. Tas,<sup>5</sup> R. B. Thayyullathil,<sup>7</sup> J. Thomas,<sup>44,48</sup> E. Tiras,<sup>24</sup> D. Torbunov,<sup>31</sup> J. Tripathi,<sup>32</sup> A. Tsaris,<sup>12</sup> Y. Torun,<sup>21</sup> J. Urheim,<sup>19</sup> P. Vahle,<sup>47</sup> J. Vasel,<sup>19</sup> L. Vinton,<sup>39</sup> P. Vokac,<sup>9</sup> T. Vrba,<sup>9</sup> B. Wang,<sup>37</sup> T. K. Warburton,<sup>24</sup> M. Wetstein,<sup>24</sup> M. While,<sup>36</sup> D. Whittington,<sup>40,19</sup> S. G. Wojcicki,<sup>38</sup> J. Wolcott,<sup>43</sup> N. Yadav,<sup>14</sup> A. Yallappa Dombara,<sup>40</sup> S. Yang,<sup>6</sup> K. Yonehara,<sup>12</sup> S. Yu,<sup>1,21</sup> J. Zalesak,<sup>23</sup> B. Zamorano,<sup>39</sup> and R. Zwaska<sup>12</sup>

(The NOvA Collaboration)

<sup>1</sup>Argonne National Laboratory, Argonne, Illinois 60439, USA

<sup>2</sup>Universidad del Atlantico, Km. 7 antigua via a Puerto Colombia, Barranquilla, Colombia

<sup>3</sup>Department of Physics, Institute of Science, Banaras Hindu University, Varanasi, 221 005, India

<sup>4</sup>California Institute of Technology, Pasadena, California 91125, USA

<sup>5</sup>Charles University, Faculty of Mathematics and Physics, Institute of Particle and Nuclear Physics, Prague, Czech Republic

<sup>6</sup>Department of Physics, University of Cincinnati, Cincinnati, Ohio 45221, USA

<sup>7</sup>Department of Physics, Cochin University of Science and Technology, Kochi 682 022, India

<sup>8</sup>Department of Physics, Colorado State University, Fort Collins, CO 80523-1875, USA

<sup>9</sup>Czech Technical University in Prague, Brehova 7, 115 19 Prague 1, Czech Republic

<sup>10</sup>University of Dallas, 1845 E Northgate Drive, Irving, Texas 75062 USA

<sup>11</sup>Department of Physics and Astrophysics, University of Delhi, Delhi 110007, India

<sup>12</sup>Fermi National Accelerator Laboratory, Batavia, Illinois 60510, USA

<sup>13</sup>Instituto de Física, Universidade Federal de Goiás, Goiânia, Goiás, 74690-900, Brazil

<sup>14</sup>Department of Physics, IIT Guwahati, Guwahati, 781 039, India

<sup>15</sup>Department of Physics, Harvard University, Cambridge, Massachusetts 02138, USA

<sup>16</sup>Department of Physics, University of Houston, Houston, Texas 77204, USA

<sup>17</sup>School of Physics, University of Hyderabad, Hyderabad, 500 046, India

<sup>18</sup>Department of Physics, IIT Hyderabad, Hyderabad, 502 205, India

<sup>19</sup>Indiana University, Bloomington, Indiana 47405, USA

<sup>20</sup>Institute of Computer Science, The Czech Academy of Sciences, 182 07 Prague, Czech Republic

<sup>21</sup>Department of Physics, Illinois Institute of Technology, Chicago IL 60616, USA

<sup>22</sup>Inst. for Nuclear Research of Russia, Academy of Sciences 7a, 60th October Anniversary prospect, Moscow 117312, Russia

<sup>23</sup>Institute of Physics, The Czech Academy of Sciences, 182 21 Prague, Czech Republic

<sup>24</sup>Department of Physics and Astronomy, Iowa State University, Ames, Iowa 50011, USA

<sup>25</sup>Department of Physics and Astronomy, University of California at Irvine, Irvine, California 92697, USA

<sup>26</sup>Department of Physics and Electronics, University of Jammu, Jammu Tawi, 180 006, Jammu and Kashmir, India

<sup>27</sup>Joint Institute for Nuclear Research, Dubna, Moscow region 141980, Russia

<sup>28</sup>*Nuclear Physics and Astrophysics Division, Lebedev Physical Institute, Leninsky Prospect 53, 119991 Moscow, Russia*

<sup>29</sup>*Department of Physics and Astronomy, Michigan State University, East Lansing, Michigan 48824, USA*

<sup>30</sup>*Department of Physics and Astronomy, University of Minnesota Duluth, Duluth, Minnesota 55812, USA*

<sup>31</sup>*School of Physics and Astronomy, University of Minnesota Twin Cities, Minneapolis, Minnesota 55455, USA*

<sup>32</sup>*Department of Physics, Panjab University, Chandigarh, 160 014, India*

<sup>33</sup>*Department of Physics, University of Pittsburgh, Pittsburgh, Pennsylvania 15260, USA*

<sup>34</sup>*Department of Physics, University of South Alabama, Mobile, Alabama 36688, USA*

<sup>35</sup>*Department of Physics and Astronomy, University of South Carolina, Columbia, South Carolina 29208, USA*

<sup>36</sup>*South Dakota School of Mines and Technology, Rapid City, South Dakota 57701, USA*

<sup>37</sup>*Department of Physics, Southern Methodist University, Dallas, Texas 75275, USA*

<sup>38</sup>*Department of Physics, Stanford University, Stanford, California 94305, USA*

<sup>39</sup>*Department of Physics and Astronomy, University of Sussex, Falmer, Brighton BN1 9QH, United Kingdom*

<sup>40</sup>*Department of Physics, Syracuse University, Syracuse NY 13210, USA*

<sup>41</sup>*Department of Physics and Astronomy, University of Tennessee, Knoxville, Tennessee 37996, USA*

<sup>42</sup>*Department of Physics, University of Texas at Austin, Austin, Texas 78712, USA*

<sup>43</sup>*Department of Physics and Astronomy, Tufts University, Medford, Massachusetts 02155, USA*

<sup>44</sup>*Physics and Astronomy Dept., University College London, Gower Street, London WC1E 6BT, United Kingdom*

<sup>45</sup>*Department of Physics, University of Virginia, Charlottesville, Virginia 22904, USA*

<sup>46</sup>*Department of Mathematics, Statistics, and Physics, Wichita State University, Wichita, Kansas 67206, USA*

<sup>47</sup>*Department of Physics, College of William & Mary, Williamsburg, Virginia 23187, USA*

<sup>48</sup>*Department of Physics, University of Wisconsin-Madison, Madison, Wisconsin 53706, USA*

(Dated: February 1, 2019)

The cross section of neutrino-induced neutral-current coherent  $\pi^0$  production on a carbon-dominated target is measured in the NOvA near detector. This measurement uses a narrow-band neutrino beam with the average neutrino energy of 2.7 GeV, which is of interest to the ongoing and future long-baseline neutrino oscillation experiments. The measured, flux-averaged cross section is  $\sigma = 14.0 \pm 0.9$  (stat.)  $\pm 2.1$  (syst.)  $\times 10^{-40}$  cm<sup>2</sup>/nucleus, consistent with model prediction. This result is the most precise measurement of neutral-current coherent  $\pi^0$  production in the few-GeV neutrino energy region.

Neutrinos can interact coherently with target nuclei and produce outgoing pions via either neutral-current (NC) or charged-current (CC) interactions. In the case of an NC interaction, a  $\pi^0$  is produced:

$$\nu A \rightarrow \nu A \pi^0. \quad (1)$$

Coherent interactions are characterized by very small momentum transfer to the target nucleus with no exchange of quantum numbers, while the target nucleus remains in its ground state. The characteristic signal topology of NC coherent  $\pi^0$  production is a single, forward-going  $\pi^0$ , with no other hadrons in the final state.

There are two major motivations for measuring the NC coherent  $\pi^0$  cross section. First, coherent  $\pi^0$  production is a contribution to the background of long-baseline  $\nu_\mu \rightarrow \nu_e$  oscillation measurements. In some neutrino detectors, the photons from  $\pi^0$  decay are reconstructed as electromagnetic showers which are often difficult to separate from the showers induced by electrons. An NC  $\pi^0$  event can be misidentified as a  $\nu_e$ -CC signal event if the two photon showers are not spatially separated, or if one shower is undetected. Knowledge of coherent  $\pi^0$  production provides a constraint on the size of this background. Second, coherent pion production provides insight into the weak hadronic current structure and a test of the Partially Conserved Axial Current (PCAC) hypothesis [1]. Models based upon PCAC relate the coherent pion production to the pion-nucleus elastic scat-

tering cross section at the  $Q^2 = 0$  limit and extrapolate to low but non-zero  $Q^2$  values. Such models include the Rein-Sehgal (RS) model [2, 3] in the GENIE neutrino generator [4] used for this analysis. Further improvement of PCAC models was made by Berger *et al.* (Berger-Sehgal model) [5] and others [6–10]. The PCAC models are known to perform well in their intended multi-GeV energy ranges. Their performance in NC interactions at neutrino energy of a few GeV however remains to be established. There is another class of models, referred to as microscopic models, that do not rely on PCAC. These models are built using pion production amplitudes at the nucleon level [11–15] and are expected to be more reliable than PCAC-based models at neutrino energies below 1 GeV.

The NC coherent  $\pi^0$  cross section contributes roughly 1% of the inclusive neutrino interactions in the few-GeV neutrino energy region, much smaller than other  $\pi^0$  production modes. This challenging situation requires extracting a small signal with large backgrounds. The backgrounds arise mainly from NC-induced baryon resonance (RES) interactions, and  $\pi^0$  production from NC deep-inelastic scattering (DIS) interactions, where only a single  $\pi^0$  is reconstructed. Diffractive (DFR)  $\pi^0$  production, where neutrinos coherently scatter off free protons (hydrogen) and produce  $\pi^0$ s, also contributes to the background. A recoil proton is often visible in DFR  $\pi^0$  production, which helps in identifying this background.

The coherent process is best identified by a low value of the square of four-momentum transfer to the nucleus ( $|t| \lesssim \hbar^2/R^2$ , where  $R$  is the nuclear radius). However, in NC interactions  $t$  cannot be determined because the outgoing neutrino momentum cannot be measured. Alternatively, distinct characteristics of the coherent process can be used to separate coherent from background  $\pi^0$  production. First, the coherent  $\pi^0$  production has no other particles in the final state and little vertex activity while background processes often produce additional nucleons or pions and have larger energy depositions near the neutrino interaction vertex. Second, the  $\pi^0$ s from coherent production are distinctly forward-going. A region with enhanced coherent signal in the 2D space of reconstructed  $\pi^0$  energy and scattering angle can be defined. The coherent signal is measured as an excess of data events over the background prediction in this region.

There are relatively few existing NC coherent  $\pi^0$  measurements. Early bubble chamber results suffer from large statistical uncertainties [16–20]. More recently, NOMAD, MiniBooNE, SciBooNE and MINOS reported coherent  $\pi^0$  measurements with higher statistics but with systematic-limited precision [21–24]. In particular, the measurements in the few-GeV neutrino energy region, relevant for the next generation neutrino oscillation experiments, have large uncertainties.

This paper reports a measurement of NC coherent  $\pi^0$  cross section using the fine-grained sampling of neutrino interactions in a predominantly carbon tracking medium afforded by the NOvA Near Detector (ND) [25] exposed to the off-axis flux of the NuMI beam [26] at Fermilab. The flux-averaged cross section is defined as

$$\sigma = \frac{N_{\text{data}} - N_{\text{bkg}}}{\epsilon \times N_{\text{target}} \times \phi}, \quad (2)$$

where  $N_{\text{data}}$  and  $N_{\text{bkg}}$  are the number of selected data and simulation-predicted background events,  $\epsilon$  is the efficiency of the coherent signal selection calculated from simulation,  $N_{\text{target}}$  is the number of target nuclei in the detector fiducial volume, and  $\phi$  is the integrated neutrino flux.

The NOvA ND consists of 193 metric tons of a fully active tracking calorimeter constructed from polyvinyl chloride (PVC) cells filled with liquid scintillator. The liquid scintillator is 62% of the fiducial mass. The target nuclei for neutrino interactions are dominantly carbon (66.7% by mass), chlorine (16.1%) and hydrogen (10.8%), with small contributions from titanium, oxygen and other nuclei. Each cell is 3.9 cm wide, 6.6 cm deep and 3.9 m in length. Cells are arranged in planes alternating between horizontal and vertical orientations to provide three-dimensional reconstruction of neutrino interactions. The fully active volume of the detector is 12.8 m in length, consisting of 192 contiguous PVC planes with 96 cells each. Each plane is approximately 0.18 ra-

diation lengths. Downstream of the fully active volume is a muon range stack with ten layers of 10 cm thick steel plates interleaved with pairs of one vertical and one horizontal scintillator plane to enhance muon containment. Scintillation light generated by charged particles passing through a cell is captured by a wavelength-shifting fiber connected to a Hamamatsu avalanche photodiode (APD) [27] at the end of the cell. The APD signals are continuously digitized, and those above a preset threshold are recorded with associated time and charge.

The NuMI neutrino beam is produced by colliding 120 GeV protons from the Main Injector accelerator on a 1.2 m-long graphite target. Charged hadrons produced in the target are focused by two magnetic horns downstream of the target to select positive mesons which then decay into neutrinos in a 675 m long decay pipe. This analysis uses data corresponding to  $3.72 \times 10^{20}$  protons-on-target (POT). The neutrino beam is simulated by FLUKA [28] and the FLUGG [29] interface to GEANT4 [30]. External thin-target hadron production measurements are used to correct and constrain the neutrino flux via the PPFX package developed for the NuMI beam by the MINERvA collaboration [31].

The NOvA ND is 1 km from the neutrino source, 100 m underground, and on average 14.6 mrad away from the central axis of the neutrino beam. The neutrino flux seen in the NOvA ND is a narrow band beam peaked at 1.9 GeV, with 68% of the flux between 1.1 and 2.8 GeV, and a mean of 2.7 GeV due to the high-energy tail. The neutrino beam in the 0 to 120 GeV energy region is predominantly  $\nu_\mu$  (91%), with a small contamination from  $\nu_e$  (1%) and anti-neutrinos (8%). In this measurement, the effect of anti-neutrinos in the flux is accounted for using simulation to give solely a neutrino-induced result. The predicted integrated neutrino flux from 0 to 120 GeV in the detector volume used in this analysis is  $\phi_\nu = 123.2 \pm 11.6 / \text{cm}^2 / 10^{10} \text{ POT}$ .

Neutrino interactions in the detector are simulated by the GENIE 2.10.4 neutrino event generator [4]. The Rein-Sehgal PCAC-based model is used to simulate the coherent process. To simulate NC RES and DIS events, the two major background contributions, the Rein-Sehgal model for baryon-resonance production [32] and the Bodek-Yang model [33] are used. The DFR events are modeled based upon the work of Rein [34]. The nuclear model is the Bodek-Richie relativistic Fermi gas (RFG) model with short-range nucleon-nucleon correlations [35, 36]. Final-state interactions of hadrons inside the nucleus are simulated in GENIE using an effective intranuclear cascade model [4]. GEANT4 [30] is used to simulate the detector’s response to the final-state particles from neutrino interactions. The propagation of photons produced by the simulated energy depositions, the response of the APDs, and the digitization of the resulting waveform is accomplished with a custom simulation package.

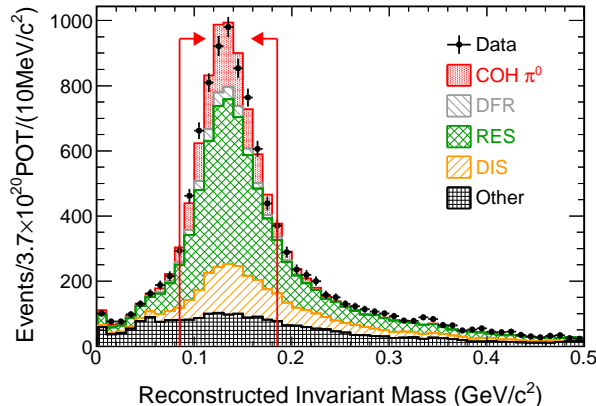


FIG. 1: Data and simulated  $\pi^0$  invariant mass distribution of the selected 2-prong NC  $\pi^0$  sample. Data are shown as solid circles with statistical error bars. The shaded histograms represent the simulated prediction divided by interaction modes, including coherent signal and NC RES, DIS and DFR background  $\pi^0$  productions. Charged current  $\pi^0$  production, external events, and interactions without final-state  $\pi^0$ s are classified under “Other”. Vertical lines with arrows show the range of invariant masses accepted into the analysis.

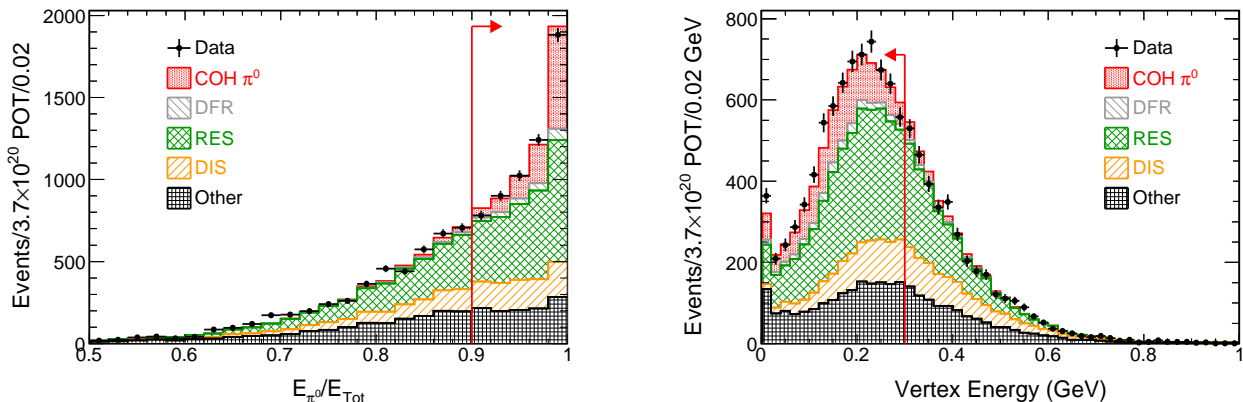


FIG. 2: Fraction of event energy contained in the reconstructed  $\pi^0$  (left) and vertex energy (right) in data (black circle) and simulation (shaded histograms). Statistical error bars are shown for data. The simulated distribution is classified by interaction modes. Events to the right (left) of the vertical red line are selected into the signal sample. The cut values are optimized by maximizing Figure of Merit ( $FoM = s/\sqrt{s+b}$ , where  $s$  and  $b$  are the numbers of signal and background events passing the cuts).

In both data and simulation, the recorded cell signals (hits) in the NOvA detector are first collected into groups by their space and time information. Each collection of hits is assumed to come from a single neutrino interaction. The intersection of the particle paths found in the collection using a Hough transform [37] are taken as seeds to find the interaction vertex. Hits are further clustered into “prongs” with defined start points and directions emanating from the vertex. Each prong contains hits attributed to one particle.

The events selected by this analysis are required to have exactly two reconstructed prongs contained in the

fully active volume of the detector, both identified as electromagnetic (EM)-like showers by log-likelihood functions based upon  $dE/dx$  information in both the longitudinal and transverse directions of the prongs [38, 39]. A Convolutional Neural Network (CVN) trained for NC/CC separation [40] is used to reject CC events. The energy of the prong is calculated as the sum of the calibrated energy deposited in each cell. The invariant mass is calculated from the momenta and opening angle of the reconstructed prongs assuming both are photons, as

$$M_{\gamma\gamma} = \sqrt{2E_{\gamma 1}E_{\gamma 2}(1 - \cos\theta_{\gamma\gamma})}, \quad (3)$$

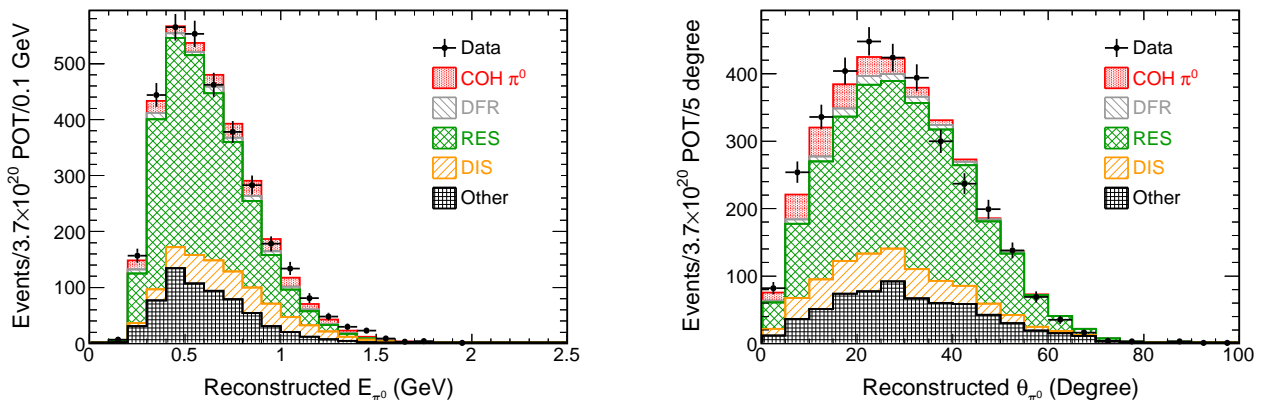


FIG. 3: Reconstructed  $\pi^0$  energy (left) and angle with respect to beam (right) of the control sample events after the background fit.

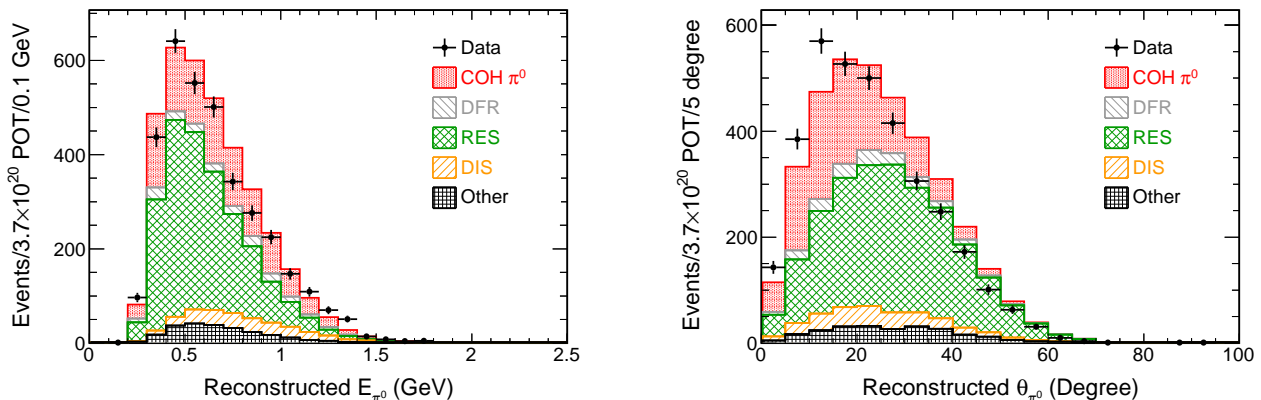


FIG. 4: Reconstructed  $\pi^0$  energy (left) and angle with respect to beam (right) of the signal sample events. The simulated backgrounds are normalized by the control sample data.

where  $E_{\gamma_1}$  and  $E_{\gamma_2}$  are the energies of the two prongs and  $\theta_{\gamma\gamma}$  is the opening angle between them. The energy scales of data and simulated events are tuned independently so that the mass peaks match the  $\pi^0$  mass ( $134.977 \text{ MeV}/c^2$ ) [41]. Only events with reconstructed  $\pi^0$  mass between 85 and 185  $\text{MeV}/c^2$  are selected to reduce backgrounds. The momenta of the two reconstructed prongs are summed up to obtain the reconstructed momentum of the  $\pi^0$ .

As shown in Fig. 1, the selected events are high-purity NC  $\pi^0$ s (90%), including both coherent signal and background arising from NC RES and DIS, with small contributions from DFR  $\pi^0$  production and other interactions. The background events may have extra energy, especially in the vertex region, but not enough to be reconstructed as prongs. To better control the background, the NC  $\pi^0$  sample is further divided into two sub-samples using

kinematic variables: the ratio of the calorimetric energy included in the reconstructed  $\pi^0$  to the total energy in the event ( $E_{\pi^0}/E_{\text{Tot}}$ ), and the energy in the vertex region defined as the first eight planes from the reconstructed interaction vertex ( $E_{\text{Vtx}}$ ). The signal-enhanced sample is defined as events with most of their energy in the 2 photon prongs ( $E_{\pi^0}/E_{\text{Tot}} > 0.9$ ) and low vertex energy ( $E_{\text{Vtx}} < 0.3 \text{ GeV}$ ) to include most of the coherent signal and reduce background. The rest of the events are defined as a control sample, dominated by  $\pi^0$ s produced by RES and DIS interactions. The signal and control sample selection is shown in Fig. 2.

The control sample data are used to constrain the background prediction. The simulated distributions of RES and DIS events in the  $\pi^0$  energy and angle ( $\cos\theta$  with respect to the average beam direction) 2D space are

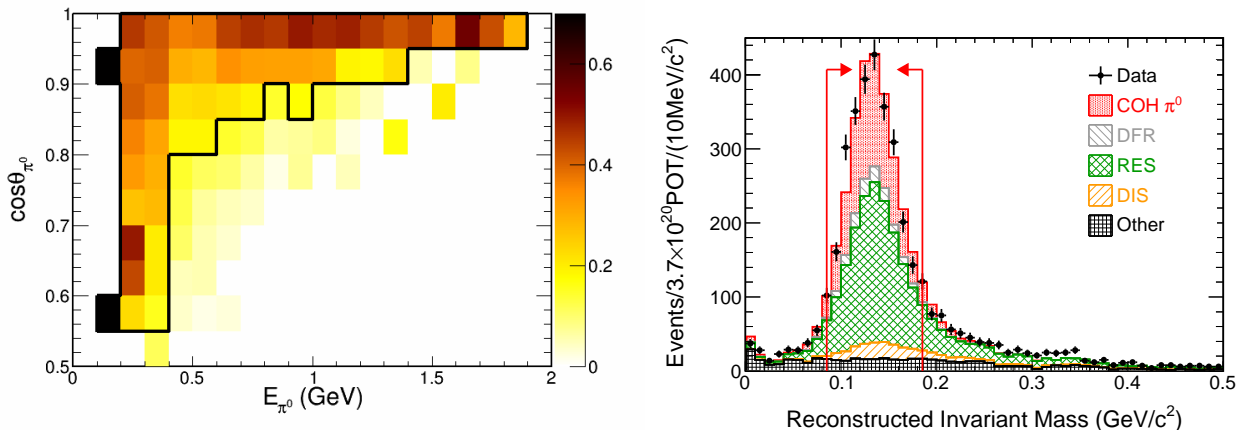


FIG. 5: Left: Ratio of coherent  $\pi^0$  signal to total simulated events in the signal sample in the 2D space of  $\pi^0$  energy and  $\cos\theta$ . The region inside the lines is the coherent region defined as bins with  $> 15\%$  of total MC being coherent  $\pi^0$ . Right:  $\pi^0$  invariant mass of the signal sample events in the coherent region as described by the left plot with the background normalized by the control sample data. Vertical lines with arrows show the range of invariant masses accepted into the analysis.

used as templates and scaled to fit the control sample data. RES and DIS have distinct  $\pi^0$  energy and angle distributions, and together they account for approximately 90% of the total background. The fitting parameters are the normalization factors of the templates. The other background components are kept fixed in the fit. The fit results in an increase of the selected RES background by  $17.6 \pm 6.4\%$  and a decrease in the DIS background by  $43.1 \pm 14.5\%$ . The two fitting parameters are strongly anti-correlated. The fit result is applied as a re-normalization to the background in the signal sample. It also provides a constraint on the systematic sources affecting backgrounds, which will be discussed later. The energy and angle of the  $\pi^0$ s in the control sample and the signal sample with the re-normalized backgrounds are shown in Figs. 3 and 4. There are noticeable discrepancies between the signal sample data and simulation, especially in the  $\pi^0$  angular distribution (Fig. 4, right). The  $\theta_{\pi^0}$  spectrum in the data favors production at angles closer to the beam direction than does the simulation, suggesting that the PCAC characterization of  $Q^2 = 0$  in Rein-Sehgal model needs refinement. Similar discrepancies in pion angular distributions have been reported by the MINERvA experiment in recent measurements of charged-current coherent pion production [42, 43]. Further study of systematic uncertainties is ongoing to quantitatively address the discrepancies.

A coherent region in the 2D  $\pi^0$  energy and angle space is defined as those bins with  $> 15\%$  predicted coherent  $\pi^0$  signal purity (Fig. 5, left). The selection is intentionally set loosely to reduce potential systematic uncertainties caused by the discrepancies in the  $\pi^0$  kinematic distributions mentioned previously. The invariant mass of the signal sample events are shown in Fig. 5, right. The

signal selection efficiency is 4.1% according to simulation. The normalized background in this coherent region is subtracted from data to obtain the number of measured signal events. The number of simulated signal events is then normalized to the number extracted from the data. The calculation is iterated until the resulting changes in the estimated signal and background populations become negligible. The outcome of this procedure is the coherent signal content, estimated to be  $987 \pm 67$  (stat.) events.

The systematic uncertainties for this analysis arise from the calorimetric energy scale, background modeling, coherent signal modeling, detector response to photon showers, detector simulation, particles entering the detector from external sources, and the simulation of neutrino flux. Data-driven methods are used wherever possible to establish the uncertainties.

The calorimetric energy scale is constrained to within 1% by the  $\pi^0$  invariant mass distributions of simulation and data which corresponds to a 3.4% uncertainty on the cross-section measurement. The background-related uncertainty is constrained by the control sample data through the template fit method. The variations that can arise with the template fit to background are estimated by varying the background-modeling parameters within their  $\pm 1\sigma$  ranges as assigned by GENIE and then repeating the template fit. GENIE does not provide a means to reweight the DFR background. The DFR normalization is varied by  $\pm 75\%$  based on the measurement by the MINERvA experiment [44, 45]. The uncertainty from each background-modeling parameter is defined as the maximum change in the measured signal events. The uncertainty in the coherent signal modeling results in an uncertainty of the efficiency correction. This effect is evaluated by varying the modeling parameters in the Rein-Sehgal

TABLE I: List of systematic and statistical uncertainties.

Source	Measurement Uncertainty (%)
Calorimetric energy scale	3.4
Background modeling	10.4
Coherent modeling	3.7
Photon shower response	1.1
External events	2.4
Detector simulation	2.0
Flux	9.4
Total systematic uncertainty	15.3
Statistical uncertainty	6.7
Total uncertainty	16.7

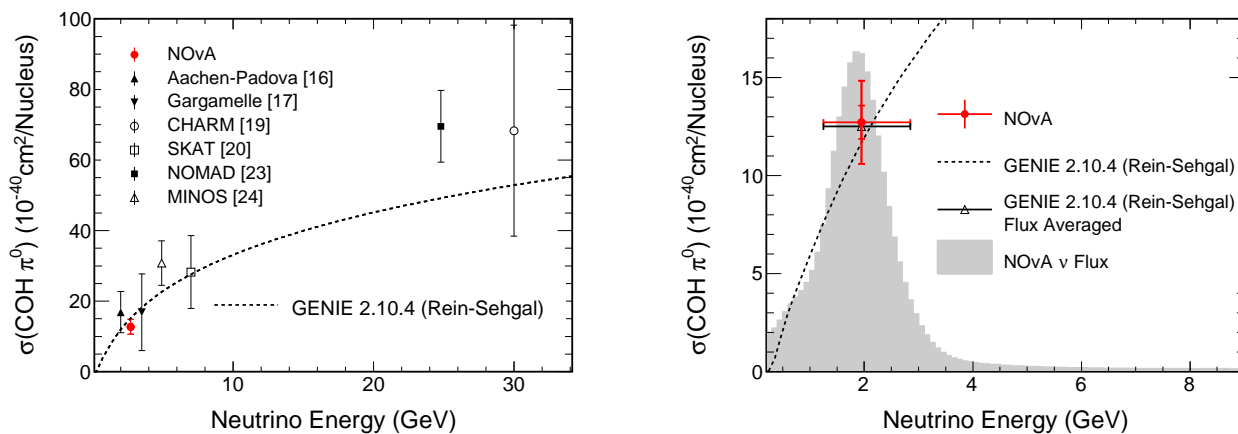


FIG. 6: Flux-averaged cross section of the NOvA NC coherent  $\pi^0$  measurement. The left plot compares this measurement to previous measurements. The neutrino energy values of the NOvA data point and other measurements are represented by an average neutrino energy. All results are scaled to a carbon target by a factor of  $(A/12)^{2/3}$  following the Berger-Sehgal model approximation, where  $A$  is the effective atomic number of the experiment. The dashed curve shows the GENIE prediction for a carbon target. The right plot compares this measurement with the GENIE predicted flux-averaged cross section from the Rein-Sehgal model. In this plot the neutrino energy of the NOvA data point is the median neutrino energy, and the horizontal error bar contains 68% of the total neutrinos. The statistical uncertainty and statistical plus systematic uncertainty are shown as vertical error bars for the NOvA result. The GENIE prediction is shown both as a function of neutrino energy, and as a flux-averaged cross section. The NOvA flux is shown in grey with arbitrary normalization.

model: axial mass ( $M_A$ ,  $\pm 50\%$ ) and nuclear radius ( $R_0$ ,  $\pm 20\%$ ) [2–4]. To check the effect of the discrepancies in  $\pi^0$  kinematic distributions on the total cross-section measurement, a test is performed by reweighting the simulated signal to data and comparing to the result obtained before reweighting. A 1% difference is found, which is negligible compared to the signal modeling uncertainty assigned. Bremsstrahlung showers induced by energetic muons from external sources provide a data-driven constraint on the simulation of detector response to photon showers. Those bremsstrahlung showers are identified and the muons are removed to create a single photon control sample in data and simulation [46]. The sample is subject to the same selection cuts as the  $\pi^0$  photons and the uncertainty is evaluated as the 1% difference be-

tween data and simulation in selection efficiency. Lastly, the neutrino flux uncertainty comes from beam focusing and hadron production with external thin-target hadron production data constraints applied [31]. The systematic sources and uncertainties are summarized in Table I. The dominant sources are background modeling and flux uncertainties. The total systematic uncertainty is estimated to be about 15%.

The flux-averaged cross section of NC coherent  $\pi^0$  production in this measurement is calculated using equation (2). The measured cross section is  $\sigma = 14.0 \pm 0.9(\text{stat.}) \pm 2.1(\text{syst.}) \times 10^{-40} \text{ cm}^2/\text{nucleus}$  at the average neutrino energy of 2.7 GeV. The effective atomic number  $A = 13.8$

TABLE II: Summary of NC coherent  $\pi^0$  measurements. The effective atomic number ( $A$ ) and the average neutrino energy ( $\langle E_\nu \rangle$ ) are shown for each experiment. The results are reported as total cross section per nucleus, cross-section ratios to inclusive  $\nu_\mu$ -CC, or to the prediction of Rein-Sehgal model.

Experiments	$A$	$\langle E_\nu \rangle$ (GeV)	$\sigma$ ( $10^{-40} \text{ cm}^2/N$ )	$\sigma/\sigma(\nu_\mu\text{-CC})$	$\sigma/\sigma(\text{Rein-Sehgal})$
Aachen-Padova [16]	27	2	$29 \pm 10$		
Gargamelle [17]	31	3.5	$31 \pm 20$		
CHARM [19]	20	30	$96 \pm 42$		
SKAT [20]	30	7	$79 \pm 28$	$4.3 \pm 1.5$	
15' BC [18]	20	20		$0.20 \pm 0.04$	
NOMAD [23]	12.8	24.8	$72.6 \pm 10.6$	$3.21 \pm 0.46$	
MiniBooNE [21]	12	0.8			$0.65 \pm 0.14$
SciBooNE [22]	12	0.8			$0.9 \pm 0.20$
MINOS [24]	48	4.9	$77.6 \pm 15.9$		
NOvA	13.8	2.7	$14.0 \pm 2.3$		

is calculated as

$$A = \left( \sum_i \frac{n_i}{n_{Tot}} A_i^{2/3} \right)^{3/2}, \quad (4)$$

where  $A_i$  is the atomic number of each chemical element (excluding hydrogen) and  $\frac{n_i}{n_{Tot}}$  is its fraction to the total number of nuclei in the fiducial volume. The factor  $A_i^{2/3}$  is an approximate cross-section scaling between different nuclei in accordance with the Berger-Sehgal model [5].

Figure 6 and Table II show this measurement together with other measurements and the GENIE prediction. All measurements in Figure 6 are scaled to a carbon target by a scale factor of  $(A/12)^{2/3}$  for the purpose of comparison. The flux-averaged NC coherent  $\pi^0$  cross section of this work is in agreement with the cross-section prediction of the Rein-Sehgal model (GENIE implementation), although some discrepancies in the  $\pi^0$  kinematic distributions are observed. This result is the most precise measurement of NC coherent  $\pi^0$  production in the few-GeV neutrino energy region, and the first such measurement on carbon-dominated target in this energy range. It benefits both current and future long-baseline neutrino oscillation experiments in background prediction with reduced uncertainty.

### Acknowledgements

NOvA is supported by the US Department of Energy; the US National Science Foundation; the Department of Science and Technology, India; the European Research Council; the MSMT CR, Czech Republic; the RAS, RMES, and RFBR, Russia; CNPq and FAPEG, Brazil; and the State and University of Minnesota. We are grateful for the contributions of the staffs of the University of Minnesota module assembly facility and Ash River Laboratory, Argonne National Laboratory, and Fermilab. Fermilab is operated by Fermi Research Alliance, LLC under Contract No. DeAC02-07CH11359 with the US DOE.

- [1] S. Adler, Phys. Rev. B **135**, 963 (1964).
- [2] D. Rein and L. M. Sehgal, Nucl. Phys. B **223**, 29 (1983).
- [3] D. Rein and L. M. Sehgal, Phys. Lett. B **657**, 207 (2007).
- [4] C. Andreopoulos *et al.*, Nucl. Instrum. Meth. A **614**, 87 (2010); C. Andreopoulos *et al.*, arXiv:1510.05494v1 [hep-ph] (2015).
- [5] C. Berger and L. M. Sehgal Phys. Rev. D **79**, 053003 (2009).
- [6] A. A. Belkov and B. Z. Kopeliovich, Sov. J. Nucl. Phys. **46**, 499 (1987).
- [7] B. Z. Kopeliovich, Nucl. Proc. Suppl. **139**, 219 (2005).
- [8] E. Hernandez *et al.*, Phys. Rev. D **80**, 013003 (2009).
- [9] A. Kartavtsev, E. A. Paschos, and G. J. Gounaris, Phys. Rev. D **74**, 054007 (2006).
- [10] E. A. Paschos, D. Schalla, Phys. Rev. D **80**, 033005 (2009).
- [11] S. Singh, M. Sajjad Athar, and S. Ahmad, Phys. Rev. Lett. **96**, 241801 (2006).
- [12] L. Alvarez-Ruso, L. Geng, S. Hirenzaki, and M. Vicente Vacas, Phys. Rev. C **75**, 055501 (2007).
- [13] J. Amaro, E. Hernandez, J. Nieves, and M. Valverde, Phys. Rev. D **79**, 013002 (2009).
- [14] T. Leitner, U. Mosel, and S. Winkelmann, Phys. Rev. C **79**, 057601 (2009).
- [15] E. Hernandez, J. Nieves, and M. Vicente-Vacas, Phys. Rev. D **80**, 013003 (2009).
- [16] H. Faissner *et al.* (Aachen-Padova Collaboration), Phys. Lett. B **125**, 230 (1983).
- [17] E. Isiksal *et al.* (Gargamelle Collaboration), Phys. Rev. Lett. **52**, 1096 (1984).
- [18] C. Baltay *et al.* (Columbia-BNL Collaboration), Phys. Rev. Lett. **57**, 2629 (1986).
- [19] F. Bergsma *et al.* (CHARM Collaboration), Phys. Lett. B **157**, 469 (1985).
- [20] H. J. Grabosch *et al.* (SKAT Collaboration), Z. Phys. C **31**, 203 (1986).
- [21] A. A. Aguilar-Arevalo *et al.* (MiniBooNE Collaboration), Phys. Lett. B **664**, 41 (2008).
- [22] K. Hiraide *et al.* (SciBooNE Collaboration), Phys. Rev. D **78**, 112004 (2008).
- [23] C. T. Kullenberg *et al.* (NOMAD Collaboration), Phys. Lett. B **682**, 177 (2009).
- [24] P. Adamson *et al.* (MINOS Collaboration), Phys. Rev. D **94**, 072006 (2016).



- [25] D. S. Ayres *et al.*, NOvA Technical Design Report, FERMILAB-DESIGN-2007-01.
- [26] P. Adamson *et al.*, Nucl. Instrum. Meth. A **806** (2016) 279-306, FERMILAB-PUB-15-253-AD-FESS-ND.
- [27] The NOvA APD is a custom variant of the Hamamatsu S8550, <http://www.hamamatsu.com/us/en/product/alpha/S/4112/S8550-02/index.html>.
- [28] T. T. Bohlen *et al.*, Nucl. Data Sheets **120**, 211 (2014); A. Ferrari *et al.*, Reports No. CERN-2005-10, No. INFN/TC 05/11, No. SLAC-R-773 (2005).
- [29] M. Campanella *et al.*, Tech. Rep. CERN-ATL-SOFT-99-004 (1999).
- [30] S. Agostinelli *et al.*, Nucl. Instrum. Meth. A **506**, 250 (2003); J. Allison *et al.*, IEEE Trans. Nucl. Sci. **53**, 270 (2006).
- [31] L. Aliaga *et al.* (MINERvA Collaboration), Phys. Rev. D **94**, 092005 (2016).
- [32] D. Rein and L. M. Sehgal, Annals Phys. **133**, 79 (1981).
- [33] A. Bodek, I. Park, and U.-K. Yang, Nucl. Phys. Proc. Suppl. **139**, 113 (2005).
- [34] D. Rein, Nucl. Phys. B **278**, 61 (1986).
- [35] A. Bodek and J. L. Ritchie, Phys. Rev. D **23**, 1070 (1981).
- [36] A. Bodek and J. L. Ritchie, Phys. Rev. D **24**, 1400 (1981).
- [37] L. Fernandes and M. Oliveira, Patt. Rec. **41**, 299 (2008).
- [38] E. Niner, Ph.D. Thesis, Indiana University (2015) FERMILAB-THESIS-2015-16.
- [39] K. Sachdev, Ph.D. thesis, University of Minnesota (2015), FERMILAB-THESIS-2015-20.
- [40] P. Adamson *et al.* (NOvA Collaboration), Phys. Rev. D **96**, no. 7, 072006 (2017).
- [41] M. Tanabashi *et al.* (Particle Data Group), Phys. Rev. D, **98**, 030001 (2018).
- [42] A. Higuera *et al.* (MINERvA Collaboration) Phys. Rev. Lett. **113**, 261802 (2014).
- [43] A. Mislivec *et al.* (MINERvA Collaboration), Phys. Rev. D **97**, 032014 (2018).
- [44] J. Wolcott *et al.* (MINERvA Collaboration), Phys. Rev. Lett. **117**, 111801 (2016).
- [45] J. Wolcott, Ph.D. thesis, University of Rochester (2015), FERMILAB-THESIS-2015-26.
- [46] H. Duyang (NOvA Collaboration), arXiv:1511.00351 [physics.ins-det] (2015).